

# Efficient many-jet event generation with Flow Matching

---

E. Bothmann <sup>a,c</sup> T. Janßen <sup>b,c</sup> M. Knobbe <sup>d</sup> B. Schmitzer<sup>b,e</sup> and F. Sinz<sup>b,e</sup>

<sup>a</sup>*IT Department, CERN, 1211 Geneva 23, Switzerland*

<sup>b</sup>*Campus Institute Data Science, University of Göttingen, Germany*

<sup>c</sup>*Institute for Theoretical Physics, University of Göttingen, Germany*

<sup>d</sup>*Theoretical Physics Division, Fermi National Accelerator Laboratory, USA*

<sup>e</sup>*Institute for Computer Science & Campus Institute Data Science, University of Göttingen, Germany*

*E-mail:* [enrico.bothmann@cern.ch](mailto:enrico.bothmann@cern.ch), [tjansse2@uni-goettingen.de](mailto:tjansse2@uni-goettingen.de),

[mknobbe@fnal.gov](mailto:mknobbe@fnal.gov), [schmitzer@cs.uni-goettingen.de](mailto:schmitzer@cs.uni-goettingen.de),

[sinz@uni-goettingen.de](mailto:sinz@uni-goettingen.de)

**ABSTRACT:** We apply for the first time the Flow Matching method to the problem of phase-space sampling for event generation in high-energy collider physics. By training the model to remap the random numbers used to generate the momenta and helicities of the scattering matrix elements as implemented in the portable partonic event generator PEPPER, we find substantial efficiency improvements in the studied processes. We focus our study on the highest final-state multiplicities in Drell–Yan and top–antitop pair production used in simulated samples for the Large Hadron Collider, which computationally are the most relevant ones. We find that the unweighting efficiencies improve by factors of 150 and 17, respectively, when compared to the standard approach of using a VEGAS-based optimisation. We also compare Continuous Normalizing Flows trained with Flow Matching against the previously studied Normalizing Flows based on Coupling Layers and find that the former leads to better results, faster training and a better scaling behaviour across the studied multiplicity range.

---

## Contents

<b>1</b>	<b>Introduction</b>	<b>1</b>
<b>2</b>	<b>Problem statement: Phase-space sampling</b>	<b>3</b>
2.1	Phase-space sampling in mathematical terms	3
2.2	Unweighted event generation through rejection sampling	4
2.3	Remapping on the unit hypercube	5
2.4	Phase-space sampling in high-energy physics	8
<b>3</b>	<b>Background: Continuous Normalizing Flows</b>	<b>10</b>
3.1	Flows from time-dependent vector fields	10
3.2	Simulation-free training with Flow Matching	12
3.3	Helicity conditioning	14
<b>4</b>	<b>Application to LHC event sample production</b>	<b>15</b>
4.1	CHILI phase-space mapping	15
4.2	PEPPER event generator	16
4.3	Event generation parameters	17
4.4	Model and training parameters	17
4.5	Evaluation	19
<b>5</b>	<b>Results</b>	<b>19</b>
<b>6</b>	<b>Conclusion</b>	<b>23</b>
<b>A</b>	<b>Event generation runcards</b>	<b>24</b>
<b>B</b>	<b>Additional figures</b>	<b>25</b>

---

## 1 Introduction

The excellent experimental precision of the current and future runs at the Large Hadron Collider (LHC) and its successors must be met with a corresponding increase in the precision of theoretical simulations. This is essential to meet the objectives outlined in collider physics programs. Otherwise the uncertainty of many experimental results would be dominated by the uncertainty of the simulated data samples that enter experimental analyses in many ways, most prominently to provide background estimates [1–5]. Precision must be improved across three key areas: parametric accuracy, numerical stability, and statistical precision. In this contribution, we focus on the latter, i.e. the challenge to deliver large simulated data samples that match the statistical quality of the experimental data. To illustrate the

scale of this challenge, the ATLAS collaboration estimates [6] that 330 billion simulated events are required to match the HL-LHC dataset for a key background process vector boson production in association with additional jets, when using the general-purpose event generator SHERPA v2.2.11. This translates to 3.8 million HEPSPC06 years [6], which corresponds to about 1000 Perlmutter  $2\times$ CPU nodes for an entire year [6].

At the heart of the event-generation pipeline lies the hard scattering event, which has two incoming particles for collider setups, and a fixed number of outgoing particles—up to seven in current production campaigns. Except for the experiment-specific simulation of the detector response, it is by far the most computationally demanding part of the pipeline, and therefore a prime target for performance improvements [7]. Low overall Monte-Carlo simulation efficiency is driven by the highest-multiplicity processes in the simulation, for which current simulation programs only achieve very low phase-space sampling efficiency. They typically rely on multi-channel techniques [8] combined with the adaptive sampling algorithm VEGAS (or similar *classical* Machine Learning algorithms) [9–14]. However, for processes with 7 outgoing particles, corresponding to a 19-dimensional phase space, the overall efficiency achieved with these methods can be as low as 0.01% [15], thus immensely degrading the statistical power of the generated sample.

Modern Machine Learning approaches to optimise sampling based on deep neural networks have been proposed to improve the efficiency by making use of their more flexible parametrisation. There has been a particular focus on using Normalizing Flows as a drop-in replacement for VEGAS [16–23]. For individual partonic channels, efficiency improvements of factors between 5 and 10 over VEGAS have been demonstrated for up to five final-state particles [21]. However, a systematic study which addresses the highest and most expensive multiplicities used in standard productions at the LHC is still missing.

Here, we propose for the first time to solve this issue using Continuous Normalizing Flows [24], which implement time-continuous flows through an ordinary differential equation (ODE). To avoid expensive simulation of the ODE dynamics during training, we use the Flow Matching method [25–28].<sup>1</sup> We study the performance of our approach for the computationally by far most prominent simulated processes for the LHC, i.e. lepton pair production ( $pp \rightarrow e^+e^- + \text{up to 5 jets}$ ) and top quark pair production ( $pp \rightarrow t\bar{t} + \text{up to 4 jets}$ ), utilising the fast event generation framework PEPPER [31] and its phase-space sampler CHILI [32]. This covers the entire multiplicity range of current production campaigns. We evaluate our results in several key measures, e.g. in the integration error of the generated sample, the effective sample size, and the unweighting efficiency, thereby comparing the performance of Continuous Flows with that of an unoptimised sample, with VEGAS, and with Coupling Layer-based Normalizing Flows [33–35]. We find that our new optimisation method increases the effective sample size by factors between 8.3 and 70 for the highest multiplicities studied, when compared to the conventional VEGAS-based optimisation. Crucially, our method also yields large improvements in unweighting efficiency for the highest currently relevant multiplicity. To the best of our knowledge, we are the first to condition the phase-

---

<sup>1</sup>Flow Matching has recently been studied for neural-network based generation of LHC events and off-shell effects [29, 30]. In contrast, in our study we do not model physical effects with a generative model, but use Flow Matching only to improve the simulation’s sampling efficiency.

space sampler on the helicity states of the external particles, which allows us to optimise for individual helicity amplitudes and exploit correlations between helicities and kinematic variables. We provide a minimal interface to the PEPPER event generator allowing for straight-forward integration of similar techniques in the future.

Our article is structured as follows: In section 2, we introduce the main problem we are trying to solve and bring it into the larger context of phase-space sampling in high-energy physics. We then provide a summary of Continuous Normalizing Flows and Flow Matching in section 3. In section 4 we describe our approach for applying Flow Matching to phase-space sampling for relevant LHC processes using the PEPPER event generator. The results are then presented in section 5, followed by our conclusions in section 6.

## 2 Problem statement: Phase-space sampling

In this section, we give an overview of phase-space sampling in high-energy physics. In order to make it more accessible to readers that are not domain experts, we begin our description in section 2.1 in mathematical terms by formulating the problem as an integral to be estimated by importance sampling. Section 2.2 introduces unweighted event generation as a different perspective motivated by typical HEP applications. In both cases, integration and unweighting, a trainable remapping from a uniform distribution to a nonuniform one can improve the relevant metrics. This is described in section 2.3, where we also derive the respective training objectives to be minimised. Finally, the connection of the mathematical treatment to physics and the discussion of domain-specific aspects follow in section 2.4.

### 2.1 Phase-space sampling in mathematical terms

The main problem is to evaluate the integral

$$I = \int_M dx p(x) f(x) \quad (2.1)$$

over a manifold  $M$ . In our application, the variable  $x$  is a vector that describes a scattering event by incorporating the momentum components of the involved particles. The probability density function  $p$  describes the probability of a scattering event through the relation  $p(x) dx = \sigma^{-1} d\sigma$ , where  $\sigma$  is the scattering cross section, and the function  $f$  gives the value of the physical observable.

Our approach to solve this problem is Monte Carlo integration using importance sampling. To make the problem more suitable for Monte Carlo sampling, we pull back  $p$  to the unit hypercube  $U = [0, 1]^d$  using a bijective map  $\phi : U \rightarrow M$ , such that

$$I = \int_0^1 d^d x \det \left[ \frac{\partial \phi}{\partial x}(x) \right] p(\phi(x)) f(\phi(x)) = \int_0^1 d^d x p_0(x) f(\phi(x)), \quad (2.2)$$

where we introduced the density  $p_0$  as the pull-back of  $p$  by  $\phi$ :

$$p_0(x) = \phi^* p(x) = p(\phi(x)) \det \left[ \frac{\partial \phi}{\partial x}(x) \right]. \quad (2.3)$$

In consequence, we can draw  $N$  points  $x_i$  independently from the multivariate uniform distribution  $u_d$  over  $U$  and approximate the integral  $I$  with the Monte Carlo estimator

$$E = \frac{1}{N} \sum_{i=1}^N p_0(x_i) f(\phi(x_i)) = \frac{1}{N} \sum_{i=1}^N w_i. \quad (2.4)$$

We call  $w_i$  the weight of the event with index  $i$ . The expectation of  $E$  is  $I$  and its variance is given by

$$\text{Var}(E) = \mathbb{E}(E^2) - \mathbb{E}(E)^2. \quad (2.5)$$

In a Monte Carlo simulation, it can be estimated by the unbiased sample variance. The variance is an indicator of the sampling efficiency. When the variance is large, many points are needed to determine the integral with a given precision. The size of the variance depends on the quality of the map  $\phi$ .

## 2.2 Unweighted event generation through rejection sampling

A related task is the production of independent and identically distributed events following the distribution with density function  $p(x)$ . In the context of HEP simulations, this is commonly called unweighted event generation. The need for it arises in the typical simulation toolchain used in experimental analyses. The parton-level event generation as described in section 2.4 is followed by further post-processing steps. These can be very expensive, especially the simulation of the detector response. If we were to use the points  $\phi(x_i)$  generated by importance sampling as described above, some of them would come with small weights. Running the post-processing on these events would consume significant resources, although their contribution to the integral is small. Consequently, generating unweighted parton-level events first is often more efficient, even though they are much more expensive to produce. Another advantage is that the sample is typically much smaller after unweighting, which saves storage space.

A general method to generate unweighted events is *rejection sampling* [36]. It can be used in the situation where it is desired to sample from the distribution  $p$  on  $M$  but one can originally only sample from another distribution  $q$ . In our case, we can sample from the uniform distribution  $u_d$  on  $U$  and apply the map  $\phi$  to find  $q(x) = \phi_* u_d(x)$ , where we introduced the push-forward operator

$$\phi_* u_d(x) = u_d(x) \det \left[ \frac{\partial \phi^{-1}}{\partial x}(x) \right] = \det \left[ \frac{\partial \phi^{-1}}{\partial x}(x) \right]. \quad (2.6)$$

Trial events are drawn from  $u_d$  and accepted or rejected based on an event-wise acceptance probability, given by

$$p_{\text{accept}}(x) = \frac{w(x)}{C} \quad \text{with} \quad w(x) = \frac{p_0(x)}{u_d(x)} = \frac{p(\phi(x))}{q(\phi(x))}, \quad (2.7)$$

where  $C$  is a scaling constant chosen such that

$$C \geq w(x) \quad \forall x \in M. \quad (2.8)$$

This procedure generates a sample of reduced size with uniform weights  $w$ , with a distribution which is identical to the target distribution. The resulting *unweighting efficiency* is given by the average acceptance probability,

$$\epsilon = \frac{\langle w \rangle}{C}, \quad (2.9)$$

which is therefore a crucial figure of merit to measure the performance of a phase-space generator. The highest efficiency can be reached by choosing  $C = w_{\max} := \max_x w(x)$ . In practice, the maximal weight  $w_{\max}$  needs to be estimated in an initial survey phase from a finite set of events. Since the unweighting efficiency is very sensitive to single large outlier weights in this survey, one often defines an effective  $w_{\max, \text{eff}}$  to increase the efficiency and to render its value more numerically stable. When encountering events with weights  $w > w_{\max, \text{eff}}$ , the event weight is set to  $w/w_{\max, \text{eff}}$ . Such weights are referred to as overweights. Choosing a suitable effective maximal weight requires balancing the introduced variance of overweights with the improved unweighting efficiency of a reduced maximal weight. A common approach is to define the desired fraction of overweight events via their contribution to the integral. For example  $\epsilon_{0.01}$  denotes the unweighting efficiency for which maximally 1% of the integral is contributed by events with weights that are larger than  $w_{\max, \text{eff}}$ .

Another frequently quoted measure to quantify the quality of a sample is the Kish effective sample size  $N_{\text{eff}}$ , defined as

$$N_{\text{eff}} = \frac{\langle w \rangle^2}{\langle w^2 \rangle}. \quad (2.10)$$

This estimates the relative size of the corresponding unit weight sample that would result in the same variance of the integral estimator [37]. Note that  $N_{\text{eff}} = 1$  if all weights are equal, i.e. if the weight distribution is given by  $\delta(w - \langle w \rangle)$ . For a narrow weight distribution, the value of  $N_{\text{eff}}$  will still be close to one, while the value becomes smaller and approaches zero for wider distributions. In contrast to the unweighting efficiency,  $N_{\text{eff}}$  is less sensitive to large outlier weights.

### 2.3 Remapping on the unit hypercube

All measures introduced above, the variance of the integral estimate, the unweighting efficiency, and the effective sample size, depend on the quality of the map  $\phi$ . The map  $\phi$  can be constructed for specific scattering processes based on physics: A well-chosen  $\phi$  incorporates knowledge about the modes and general shape of  $p$  (and possibly  $f$ ). Although  $\phi$  can be designed manually for simple cases, finding an effective mapping becomes challenging for more complex scattering processes, especially those involving many particles. This leads to large variances in eq. 2.5 and small unweighting efficiencies in eq. 2.9. To address this problem, we use optimisation techniques and combine  $\phi$  with a second bijective map,  $\psi_\theta : U \rightarrow U$ , a parametric model with parameters  $\theta$  that can be adapted to data. This is visualised in figure 1.

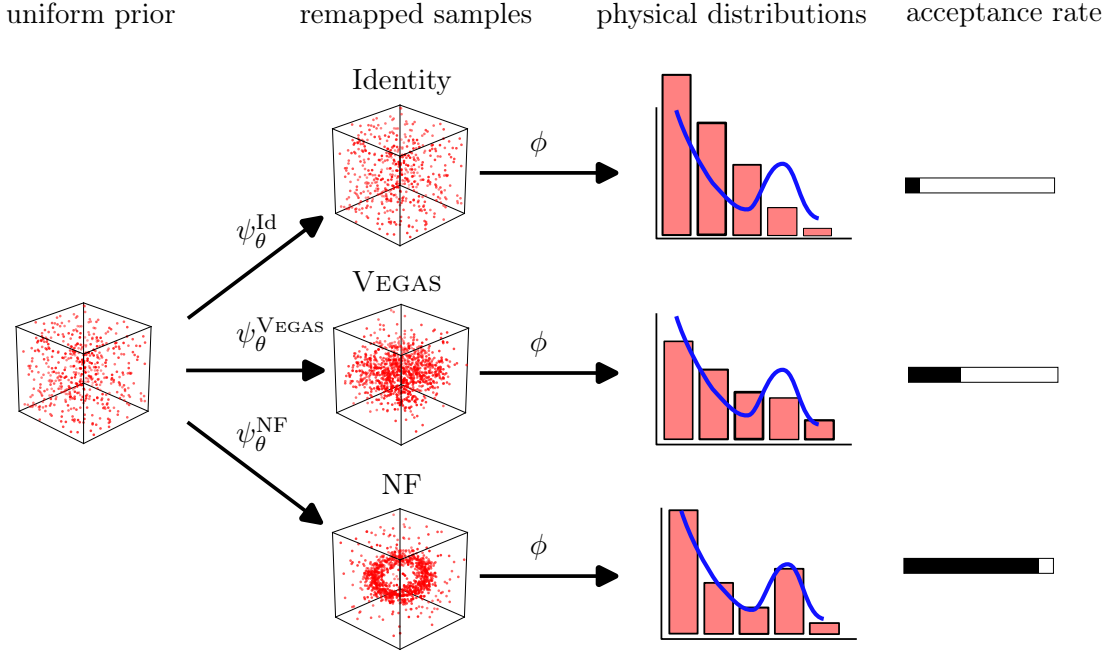


**Figure 1.** Visualisation of the maps used in our integration approach. Beginning from the uniform prior,  $\psi_\theta$  remaps the random numbers and  $\phi$  maps to the physical variables. The latter are represented after a projection onto a one-dimensional physical distribution, with the true distribution depicted as a solid line. The Monte-Carlo acceptance rate depends on how similar the generated and the true distribution are.

We first consider the case of integration, as described in section 2.1. After introducing the map  $\psi_\theta$ , the integral eq. 2.2 becomes

$$I = \int_0^1 d^d x \left| \frac{\partial \psi_\theta}{\partial x} \right| p_0(\psi_\theta(x)) f(\phi(\psi_\theta(x))) \quad (2.11)$$

and its Monte Carlo estimator is now given by

$$E_\theta = \frac{1}{N} \sum_{i=1}^N \left| \frac{\partial \psi_\theta}{\partial x} \right| p_0(\psi_\theta(x_i)) f(\phi(\psi_\theta(x_i))). \quad (2.12)$$

Its expectation value is  $\langle E_\theta \rangle = I$  by definition and its variance is

$$\text{Var}(E_\theta) = \mathbb{E}(E_\theta^2) - \mathbb{E}(E_\theta)^2. \quad (2.13)$$

Let

$$q_\theta = (\psi_\theta)_* u_d. \quad (2.14)$$

The variance, eq. 2.13, becomes minimal when  $q_\theta$  is proportional to  $p_0 \cdot (f \circ \phi)$ . Thus, if our goal is to minimise the variance, we need to optimise  $\psi_\theta$  such that  $q_\theta$  becomes close to  $p_0 \cdot (f \circ \phi)$ . If the integral is the total scattering cross section  $\sigma$ , the function  $f$  is constant and the task reduces to finding a  $q_\theta$  close to  $p_0$ .

We can also consider unweighted event generation, cf. section 2.2, with  $\psi_\theta$ . In this case, we sample from  $q_\theta$  and accept events with probability

$$p_{\text{accept}}(x) = \frac{w_\theta(x)}{C_\theta} \quad \text{with} \quad w_\theta(x) = \frac{p_0(x)}{q_\theta(x)}, \quad (2.15)$$

where the ideal scaling factor is now  $C_\theta = \max_x w_\theta(x)$ . The unweighting efficiency, eq. 2.9, becomes

$$\epsilon_\theta = \frac{\langle w_\theta \rangle}{C_\theta}. \quad (2.16)$$

The highest unweighting efficiency is reached when  $q_\theta$  is equal to  $p_0$ . In that case, all weights have a value of one and all events are accepted. Therefore, in order to maximise the unweighting efficiency, we need to optimise  $\psi_\theta$  such that  $q_\theta$  becomes close to  $p_0$ . This is the same target as for reducing the variance of the integral estimator in the case that  $f$  is constant. The precise metric is different, however. For variance minimisation, we minimise the square loss  $\mathbb{E}(E_\theta^2)$  in eq. 2.13, while for unweighting we minimise  $\max_x w_\theta(x)$ , which determines the unweighting efficiency  $\epsilon_\theta$  in eq. 2.16. In other words, for unweighting we are first and foremost interested in a reduction of the maximum weight, while the variance cares about the average deviation from the mean. Note that in unweighting, it can be beneficial to intentionally overpopulate specific regions of phase-space. This can happen, for example, when an event sample is meant to be used for several different analyses (looking at different observables  $f$ ) and one of them needs a large number of events in the tail of some observable. If such an ‘‘enhancement’’ should be done with respect to an observable  $f$ , it can be achieved by multiplying it to the event weight:  $w_\theta^{\text{enh}}(x) = f(\phi(x)) \cdot w_\theta(x)$ . In that case, the optimal  $q_\theta$  is proportional to  $p_0 \cdot (f \circ \phi)$ , just as for the integration case.

A basic example of  $\psi_\theta$  is the Vegas algorithm, an adaptive importance sampler that factorises the problem into one-dimensional, piecewise-linear maps. The key idea of VEGAS is to construct  $\psi_\theta$  as a product deformation map

$$\psi_\theta^{\text{VEGAS}}(x) = \prod_{j=1}^d \psi_j(x_j), \quad (2.17)$$

where  $x_j$  denotes the  $j$ th component of the vector  $x$  and  $\prod$  is the Cartesian product. The one-dimensional maps  $\psi_j$  are piecewise linear and can be adapted by varying the widths of the linear segments. In a Monte-Carlo simulation, the adaption is typically performed in an initial optimisation phase, and the bin widths are optimised such that the variance is distributed equally among the bins. The density  $q_\theta^{\text{VEGAS}} = (\psi_\theta^{\text{VEGAS}})_* u_d$  is piecewise constant. Therefore, sampling can be performed by selecting a bin randomly and sampling uniformly between the bin edges.

While VEGAS can achieve large improvements in variance and unweighting efficiency in practice, it can fall short if  $p_0$  does not factorise. This can be alleviated by realising  $q(x) = \phi_* u_d(x)$  as a mixture density  $q(x) = \sum_i \alpha_i q_i(x)$ , where the components  $q_i$  exploit known factorisations of individual terms contributing to the target function  $p(x)f(x)$ . This *multi-channel* approach, in combination with an optimisation of the mixture weights  $\alpha_i$  [8]

and a VEGAS remapping of each component  $q_i$  [10], is the de facto state of the art in HEP. However, phase-space sampling is still a major challenge for complex scattering processes.

A more expressive alternative to VEGAS is given by Normalizing Flows [33, 38, 39], which use neural networks to parameterise  $\psi_\theta$ . Through restrictions in their architecture, Normalizing Flows can be designed in a way so that their Jacobian determinant is tractable without having to invert the neural networks. Flows based on Coupling Layers [33], for example, implement the flow as a chain of discrete, simpler steps. In this work, we propose to realise  $\psi_\theta$  as a Continuous Normalizing Flow [24], where the map is constructed implicitly by integrating a time-dependent vector field, which is implemented by a neural network. We argue that Flow Matching [25–28] is a useful training method for the CNF, since it does not require to numerically solve an ODE during training. We compare this method with Normalizing Flows based on Coupling Layers, and with the VEGAS algorithm, which is the default method used in the PEPPER event generator and therefore serves as our baseline. We demonstrate in section 5 that the CNF is stable to train and outperforms the other approaches for the most challenging, i.e. highest dimensional, examples.

## 2.4 Phase-space sampling in high-energy physics

A central quantity in HEP simulations is the scattering cross section, which is a direct measure of the probability of the given process to occur. For hadronic collisions, e.g. at the LHC, it is given by

$$\sigma_{h_1 h_2 \rightarrow X} = \sum_{i,j} \int_0^1 dx_1 \int_0^1 dx_2 f_i(x_1, \mu_F) f_j(x_2, \mu_F) \hat{\sigma}_{ij \rightarrow X}(x_1, x_2, \mu_R, \mu_F), \quad (2.18)$$

where the sum runs over all possible partons found within the incoming hadrons  $h_{1,2}$ , i.e. quarks, antiquarks, and gluons. The individual partonic contributions (called subprocesses) can be integrated separately. This means we can ignore the sum for now and concentrate on a single subprocess. The integration is performed over  $x_{1,2}$ , the light-cone momentum fractions of the partons  $i, j$ . Finally, we have the renormalisation- and factorisation scales  $\mu_{R,F}$  and the functions  $f_{i,j}$ , which are called parton distribution functions (PDFs). They can not be calculated from first principles and thus have to be determined from data. Typically, they are provided as precomputed grids in  $x$  and  $\mu_F^2$  and values between the knots are obtained using cubic interpolation. The PDFs are nonlinear and vary over several orders of magnitude.

The remaining ingredient of eq. (2.18) is the partonic cross section  $\hat{\sigma}_{ij \rightarrow X}$ , which is an integral over the final-state four-momenta  $p_f = (E_f, \vec{p}_f)$ , with  $f = 3, \dots, m$  and  $m$  being the number of incoming and outgoing particles. As a differential, it is given by

$$\begin{aligned} d\hat{\sigma}_{ij \rightarrow X} &= \frac{1}{2E_1 E_2 |\vec{v}_1 - \vec{v}_2|} \left( \prod_f \frac{d^3 \vec{p}_f}{(2\pi)^3} \frac{1}{2E_f} \right) \\ &\times \left| \mathcal{M}_{ij \rightarrow X}(p_1, p_2 \rightarrow \{p_f\}) \right|^2 (2\pi)^4 \delta^{(4)} \left( p_1 + p_2 - \sum_{k=3}^m p_k \right) \Theta(\{p_f\}). \end{aligned} \quad (2.19)$$

We include the discontinuous cut function  $\Theta$ , which depends on the final-state momenta, and assumes either the value 0 or 1. This implements the phase-space cuts, which are discussed in more details below. The squared matrix element,  $|\mathcal{M}_{ij \rightarrow X}|^2$ , is evaluated in perturbation theory, and is a complicated function that depends on the partonic process,  $ij \rightarrow X$ , and the incoming and outgoing particle momenta:

$$\left| \mathcal{M}_{ij \rightarrow X}(p_1, p_2 \rightarrow \{p_f\}) \right|^2 \propto \sum_{\lambda_1, \dots, \lambda_d} \mathcal{A}^{\lambda_1, \dots, \lambda_m}(p_1, \dots, p_m) \mathcal{A}^{\lambda_1, \dots, \lambda_m}(p_1, \dots, p_m)^\dagger, \quad (2.20)$$

where most of the structure is expressed in the helicity amplitudes  $\mathcal{A}$ . Here, the helicity amplitudes include the external polarisation vectors and spinors for the external helicities  $\lambda_i$ , and all required colour factors. Certain helicity configurations  $\lambda_1, \dots, \lambda_d$  can result in vanishing  $\mathcal{A}$ . These vanishing configurations can easily be identified before the sampling begins and can then be ignored therein. The number of non-vanishing helicity configuration is referred to as  $n_{\text{hels}}$  throughout this work.

The remaining component is the Lorentz-invariant phase space, which is needed to implement the symmetries of the system. These reduce the dimensionality of the partonic cross section from  $4n_{\text{out}}$  (with  $n_{\text{out}} = m - 2$  being the number of outgoing particles) to  $3n_{\text{out}} - 4$ . Together with the integrals over  $x_{1,2}$ , the total dimensionality is  $d = 3n_{\text{out}} - 2$ . For the LHC, Monte-Carlo simulations typically have  $n_{\text{out}} \lesssim 7$ , such that  $d \lesssim 19$ .

The result of the integral for  $\sigma$  in eq. (2.18) is needed for overall normalisation, but can usually be estimated with sufficient accuracy without too much computational effort, at least at leading and next-to-leading order in perturbation theory. The real computational challenge lies in generating large event samples distributed according to  $d\sigma$  in this high-dimensional phase space. They have to contain sufficiently many events to allow for flexible statistical comparisons of distributions for a variety of physics observables, both in the bulk and in the tails. A good phase-space sampler must therefore be efficient throughout phase-space, across regions where the integrand varies by many orders of magnitudes.

We can now connect this discussion with the generic description in section 2.1. The manifold  $M$  is given by all possible values for the momentum fractions  $x_{1,2}$  and the final-state momenta  $\{\vec{p}_f\}$ , where the fractions assume values between 0 and 1, and the momenta are constrained by energy-momentum conservation as implemented by the delta distribution in eq. (2.19). The probability density function  $p$  is given by  $p(x)dx = \sigma^{-1}d\sigma = \sigma^{-1}dx_1 dx_2 f_i f_j d\hat{\sigma}$ , with the delta distribution removed. Finally, in eq. (2.18), we consider the special case  $f(x) = \sigma$ . However, in practice, when evaluating the integral using Monte-Carlo integration, one can store the generated sample of phase-space points and the corresponding values of  $p(x)$  and re-evaluate the integral for any  $f(x)$  in a fast and straightforward way. This flexibility is one of the main advantages of using Monte-Carlo sampling.

Now, to find an optimal map  $\psi_\theta$  in the sense defined in section 2.3, the task is to mimic the integrand of eq. (2.18) closely, to improve the estimate of the integral or the unweighting efficiency. However, its structure makes this approximation challenging. Experimental and theoretical considerations require phase-space cuts  $\Theta$  in eq. (2.19), effectively setting the matrix element to zero for certain regions. These introduce discontinuities, often in regions where the integrand is large, since such cuts are commonly applied to remove singularities.

Furthermore, with the matrix elements  $|\mathcal{M}|^2$  being comprised of products of strongly peaking helicity amplitudes, see eq. (2.20), the integrand becomes multimodal, with potentially very narrow peaks separated from each other. Finally, the integration dimensions are strongly correlated. This correlation is potentially increased by the fact that, as indicated by the delta functions in eq. (2.19), the integration is only performed over a submanifold of reduced dimensionality (as defined by the Lorentz-invariant phase space). While this manifold can be mapped out efficiently, the mapping can introduce further correlations in the process.

### 3 Background: Continuous Normalizing Flows

In this section, we describe how Continuous Normalizing Flows (CNFs) provide a viable solution to the sampling problem described in section 2.1. We begin by introducing the concept of CNFs in section 3.1. There we also show how to generate samples with the flow and how to evaluate its density. In section 3.2, we show how a CNF can be trained efficiently, without solving the flow differential equation, using the Flow Matching method. We conclude in section 3.3 with a description of how to condition the flow on inputs with discrete values, like the helicity states of external particles in a scattering event.

#### 3.1 Flows from time-dependent vector fields

As described in section 2, we want to generate samples from a target density<sup>2</sup>  $p : \mathbb{R}^d \rightarrow \mathbb{R}$  but are only able to sample from a latent density  $q_0$ . We would like to find a map  $\psi : \mathbb{R}^d \rightarrow \mathbb{R}^d$  and use it to transform samples  $x \sim q_0$  such that  $\psi(x) \sim p$ , or at least that they are close in distribution. Normalizing Flows provide such a map in the form of a parametrised diffeomorphism that can be trained on data. Methods differ in how exactly the map is constructed and which loss functional is used for training. An example are discrete-time flows based on a finite sequence of simple maps,  $\psi = \psi_k \circ \dots \circ \psi_1$ . These can be built, for example, with Coupling Layers [33] and are typically trained with a Kullback–Leibler (KL) loss. For phase space sampling in HEP, this option has been explored in refs. [17–21, 40, 41]. Below, we show how  $\psi$  can also be realised as a Continuous Normalizing Flow, which is the continuous-time analogue. As shown in section 5, we observe that CNFs are easier to train and scale better to higher dimensions than discrete-time flows.

Let  $v_t : [0, 1] \times \mathbb{R}^d \rightarrow \mathbb{R}^d$  be a smooth time-varying vector field. This vector field describes the velocity of a point  $x_t \in \mathbb{R}^d$  at time  $t \in [0, 1]$ . The motion of the point is determined by the ordinary differential equation (ODE)

$$\frac{dx_t}{dt} = v_t(x_t). \quad (3.1)$$

We denote the solution to this ODE by  $\psi_t : \mathbb{R}^d \rightarrow \mathbb{R}^d$  and the initial conditions are given by  $\psi_0(x_0) = x_0$  (or  $\psi_0 = \text{Id}$ ). The map  $\psi_t$  is the time-dependent flow of the vector field  $v_t$ . This can be used to generate samples at arbitrary times  $t$ : We sample  $x_0 \sim q_0$  and apply

---

<sup>2</sup>For simplicity in the notation, we here ignore the map  $\phi$  and drop the subscript 0 accordingly. We also ignore the function  $f$  but note that it could be added to all equations with ease.

the map  $\psi_t$ , for which we have to integrate the ODE (3.1):

$$x_t = \psi_t(x_0) = \int_0^t v_{t'}(\psi_{t'}(x_0)) dt'. \quad (3.2)$$

This allows us to determine the trajectory of any point. By the Picard–Lindelöf theorem, if  $v_t$  is Lipschitz continuous in space and continuous in time, the solution to the ODE (3.1) is unique and trajectories of different initial points never intersect, which ensures that  $\psi_t$  has an inverse.

Another quantity we are interested in is the probability density  $q_t(x_t)$  for a generated point  $x_t$  at time  $t$ . To derive this, we note that due to local conservation of probability, the density has to obey the continuity equation

$$\frac{\partial}{\partial t} q_t(x) + \nabla \cdot (q_t(x)v_t(x)) = 0. \quad (3.3)$$

Plugging in  $x = x_t = \psi_t(x_0)$ , cf. eq. (3.2), it follows that

$$\frac{d}{dt} q_t(\psi_t(x_0)) + q_t(\psi_t(x_0)) \nabla \cdot v_t(\psi_t(x_0)) = 0, \quad (3.4)$$

which simplifies to

$$\frac{d}{dt} \log q_t(\psi_t(x_0)) + \nabla \cdot v_t(\psi_t(x_0)) = 0. \quad (3.5)$$

So to evaluate  $q_t(x_t)$ , we need to solve this ODE by integrating it numerically from 0 to  $t$ . In practice, sampling and density evaluation can be done jointly by solving the system

$$\frac{d}{dt} \begin{bmatrix} \psi_t(x_0) \\ \log q_t(\psi_t(x_0)) \end{bmatrix} = \begin{bmatrix} v_t(\psi_t(x_0)) \\ -\nabla \cdot v_t(\psi_t(x_0)) \end{bmatrix} \quad (3.6)$$

with initial conditions

$$\begin{bmatrix} \psi_t(x_0) \\ \log q_t(x_0) \end{bmatrix}_{t=0} = \begin{bmatrix} x_0 \\ \log q_0(x_0) \end{bmatrix}. \quad (3.7)$$

We can also compute the density for an arbitrary point  $x_1$  at time  $t = 1$ , which has not necessarily been generated with the flow. Using an auxiliary function  $a_t$ , the appropriate reverse ODE is

$$\frac{d}{dt} \begin{bmatrix} \tilde{\psi}_t(x_1) \\ a_t \end{bmatrix} = \begin{bmatrix} -v_t(\tilde{\psi}_t(x_1)) \\ \nabla \cdot v_t(\tilde{\psi}_t(x_1)) \end{bmatrix} \quad (3.8)$$

and has to be integrated from 1 to 0 with the initial conditions at  $t=1$

$$\begin{bmatrix} \tilde{\psi}_t(x_1) \\ a_t \end{bmatrix}_{t=1} = \begin{bmatrix} x_1 \\ 0 \end{bmatrix}. \quad (3.9)$$

The auxiliary function can then be used to determine the density:

$$\log q_1(x_1) = \log q_0(x_0) - a_0. \quad (3.10)$$

Above, we have defined the domain of  $\psi_t$  to be  $\mathbb{R}^d$  instead of the unit hypercube  $U$  used in section 2.3. This is the natural way to define the flow, because it allows the vector field

$v_t$  to be unconstrained with regard to boundaries. In consequence, the natural (uninformed) base distribution is a standard normal. To map the output  $x_t$  of the flow to  $U$ , we use the element-wise sigmoid transform:

$$\text{sig} : \mathbb{R} \rightarrow [0, 1], \quad x \mapsto \text{sig}(x) = \frac{1}{1 + e^{-x}}. \quad (3.11)$$

To account for the associated change in density, we have to multiply with the corresponding Jacobian determinant.

### 3.2 Simulation-free training with Flow Matching

So far we have discussed how the map  $\psi_t$  can be constructed from a velocity field  $v_t$  to generate samples  $x_t$  and how we can evaluate the density for a given point  $x_1$ . What is still missing is a way to find a map  $\psi_t$  (or velocity field  $v_t$ ) such that the density  $q_1(x)$  closely approximates the target density  $p(x)$ . To this end, we use a model  $v_{t,\theta}$  with trainable parameters  $\theta$  to parametrise the vector field  $v_t$ . A neural network is a convenient choice for  $v_{t,\theta}$ , since eqs. (3.6) and (3.8) imply that for sampling or density evaluation, we only need to evaluate  $v_{t,\theta}$  and not its gradient or inverse. The vector field should be continuously differentiable, though.

Assume we are given training data in the form of samples  $x_1 \sim p(x)$ . We want to use these data to adapt  $v_{t,\theta}$ . Given that we can evaluate the model density  $q_{t,\theta}$ , using eqs. (3.8) and (3.10), an obvious way would be maximum likelihood estimation (MLE), i.e. minimising the KL loss between  $q_{t,\theta}(x_1)$  and  $p(x_1)$ , as proposed in [24]. However, this approach has two major drawbacks: First, training is slow because in each step the ODE (3.8) has to be integrated with a numerical ODE solver, which needs many time steps to avoid large errors from the time discretisation. Second, there is no direct gradient information for the vector field for intermediate times between 0 and 1, since only the endpoint of the flow is relevant for the KL loss. While there are approaches to regularise the flow, see e.g. refs. [42, 43], these still require simulation during training.

The drawbacks of maximum likelihood training motivated the development of simulation-free training methods [25–28]. The idea is to directly match the vector field  $v_{t,\theta}$  to a target vector field  $u_t$ , which generates the target density  $p$ . There are various ways to construct an admissible  $u_t$ . We briefly outline the strategy of refs. [25, 44] via conditional vector fields. Let

$$u_t(x \mid x_0, x_1) = x_1 - x_0, \quad (3.12)$$

with  $x_0 \sim q_0$  and  $x_1 \sim p$  being samples from the base and target distribution, respectively. Clearly, a particle starting at  $x_0$  will flow to  $x_1$  along a straight line when following  $u_t(\cdot \mid x_0, x_1)$ , i.e.

$$x_t = tx_1 + (1 - t)x_0. \quad (3.13)$$

Let now

$$u_t(x) = \mathbb{E}_{\substack{(x_0, x_1) \sim \pi, \\ x_t = x}} [u_t(x \mid x_0, x_1)]. \quad (3.14)$$

It can be shown [25, 28, 44] that the flow according to  $u_t$  transforms  $q_0$  into  $p$  as long as the marginals of the joint law  $\pi$  are  $q_0$  and  $p$ . For instance, we can set  $\pi(x_0, x_1) = q_0(x_0) \cdot p(x_1)$

(independent coupling). Note that we condition the expectation to pairs  $(x_0, x_1)$  where  $x_t$ , eq. (3.13), moves through the query point  $x$ . It is now natural to fit  $v_{t,\theta}(x)$  to  $u_t(x)$ , e.g. via

$$\mathbb{E}_{\substack{(x_0, x_1) \sim \pi, \\ t \sim U_1}} \|v_{t,\theta}(x_t) - u_t(x_t)\|^2. \quad (3.15)$$

Note that evaluating  $u_t$  at specified points  $x$  is cumbersome due to the conditioning in eq. (3.14). Fortunately, one can show [25, 44] that eq. (3.15) has the same minimisers as

$$\mathcal{L}_{\text{FM}} = \mathbb{E}_{\substack{(x_0, x_1) \sim \pi, \\ t \sim U_1}} \|v_{t,\theta}(x_t) - u_t(x_t | x_0, x_1)\|^2. \quad (3.16)$$

The flow matching objective, eq. (3.16), has attractive properties. It is local in space and time, so it can be evaluated fast and without solving an ODE. Also, in contrast to a KL loss, the minimiser is unique (on the support of the data). In consequence, sample-based training becomes easy.

More generally, one can add noise to the interpolation to increase robustness. This is done by adding noise with a small standard deviation  $\sigma_{\text{noise}}$  to the individual straight lines  $x_t$ . This way, the sampled data cover more volume. For details, see refs. [25, 44].

We note that despite using a linear interpolation in eq. (3.13), the flow trajectories  $x_t$  will in general not be straight lines. If the independent coupling is used, the samples  $x_0$  and  $x_1$  are paired randomly in eq. (3.16) and the vector field  $v_{t,\theta}$  will converge towards a local average of the interpolants. At time  $t = 1$ , it will still approximate the desired target  $p$  but when the trajectories are highly curved, sampling from the flow becomes slow because many small time steps are needed to achieve an accurate result with a numerical ODE solver. In the case of perfectly straight trajectories, a single step would suffice. Several approaches have been proposed to straighten the flow. In ref. [28], the authors propose an iterative procedure, where the first iteration uses the independent coupling and in each subsequent iteration, the coupling  $\pi$  is realised by the flow of the vector field  $v_{t,\theta}$  trained in the previous iteration. This means that  $x_0 \sim q_0$  and  $x_1 \sim q_1 = (\psi_\theta)_* q_0$  (which implies the method is not simulation-free). The authors show that each training renders the flow trajectories more straight. However, it also accumulates estimation error, since the samples are not drawn from  $p$  anymore. Therefore, the authors recommend to not apply too many iterations. Another approach is to use a coupling between  $x_0$  and  $x_1$  that already encourages straight trajectories during a single training iteration. This can be done by solving the optimal transport (OT) problem and drawing  $x_0$  and  $x_1$  from the OT plan  $\pi(x_0, x_1)$ . Since this is computationally intractable for large datasets, one can instead use a minibatch approximation where the OT plan is computed only for minibatches of data. The resulting trajectories are not perfectly straight due to the bias from the approximation but it has been shown that even small batch sizes can lead to significant straightening [44, 45]. In this work, we focus on the quality of the trained flows and do not investigate the use of straightening techniques. We note, however, that their application would be useful to reduce the sampling costs.

We make two modifications to the flow matching objective. First, in section 2.1 we have used the map  $\phi$  to map our target distribution to the unit hypercube  $U$ , which means that our training data is also defined on that domain. As noted in the previous section, the flow

is defined on  $\mathbb{R}^d$ . Our solution for sampling was to use a sigmoid transform. Here, we need to apply its inverse, the logit transform

$$\text{logit} : [0, 1] \rightarrow \mathbb{R}, \quad x \mapsto \text{logit}(x) = \ln \frac{x}{1-x}, \quad (3.17)$$

to map the training data to  $\mathbb{R}^d$ . To avoid numerical issues when the input to the logit is large in magnitude, we compose it with an affine transformation,  $x \mapsto x \cdot (1 - \epsilon) + \epsilon/2$ . We found  $\epsilon = 1 \times 10^{-6}$  to work well in our case. For sampling, the inverse transformation has to be applied accordingly.

The second modification is related to the fact that, in contrast to what is assumed in eq. (3.16), we do not sample  $x_1 \sim p$  since this is our goal in the first place. Instead, we sample from the uniform distribution  $u_d$ . We can still use the flow matching objective by multiplying it with the importance weight  $w$ , cf. eq. (2.7). This accounts for the mismatch in density. The approach is a variant of the Energy Conditional Flow Matching objective proposed in ref. [44]. Of course, the importance sampling can lead to a high variance of the Monte Carlo estimator of eq. (3.16) due to fluctuations in the weights. This is especially problematic in high dimensions. To keep this under control, it is important to use a map  $\phi$  that reduces the variance to such an extent that model training becomes feasible. This requires a deep understanding of the physics involved. After training, the flow is itself a good sampler that can be used to generate new training data with a narrower distribution of weights. This suggests an iterative training scheme, where the flow trained in one iteration is used to generate the training data by sampling from  $q_\theta = (\psi_\theta)_* u_d$  for the next iteration with weights according to (2.15). We note that VEGAS could also be used to generate the data for the first iteration. Similarly, a Markov-Chain Monte-Carlo sampler could be used [46].

### 3.3 Helicity conditioning

Normalizing Flows can be used to model conditional probability density functions. This is particularly interesting in combination with the PEPPER event generator, which allows to evaluate the sum over squared helicity amplitudes in eq. 2.20 through a Monte Carlo sampling of the non-vanishing helicity configurations. In this case, the sampling of the particle momenta can be conditioned on the discrete helicity configuration corresponding to the helicity amplitude to be evaluated. Some of the helicity configurations can be highly correlated and through the use of neural networks, Normalizing Flows can be expected to learn these correlations well. This is a clear advantage in comparison to VEGAS, which would need to adapt to each helicity configuration individually, with poor convergence expected for configurations with low probability. By default, PEPPER uses a single VEGAS map for all helicity configurations, which averages over their respective distributions.

We note that, in principle, Normalizing Flows could be conditioned on any variable. In ref. [47] this has been used for the sectors occurring in NNLO QCD calculations with the sector-improved residue subtraction method. Other examples include the different partonic channels in scattering processes with hadronic initial states and jet final states or the different multiplicities contributing to inclusive cross sections, which we will both explore in the future. Here we describe the general method.

Let  $k$  be the number of different discrete states. Each state is assigned an integer value, denoted by  $h \in 1 \dots k$ . To condition a Continuous Normalizing Flow on  $h$ , we use a conditional vector field  $v_{t,\theta}(\cdot | h)$ . By integrating the ODE, this can be used to sample from a conditional model density  $q_{1,\theta}(\cdot | h)$ . Since the vector field is implemented by a neural network, we have to use a continuous representation of  $h$  to feed the values into the network. To this end, we use an embedding layer, which is trained jointly with the vector field. The representation from the embedding layer is then concatenated to the other input variables and fed into the input layer of the network. The non-vanishing helicity configurations themselves are sampled randomly, with weights determined from training data by their respective contribution to the integral.

## 4 Application to LHC event sample production

Here we present our approach for applying our novel neural network optimisation method to single partonic channels in two standard-candle processes at the LHC, lepton and top pair production in association with additional jets, at a centre-of-mass energy of  $\sqrt{s} = 13$  TeV. For both processes, we focus on the single partonic channel that contributes most of the overall cross section, which is  $d\bar{d} \rightarrow e^+e^- + ng$  for lepton pair production and  $gg \rightarrow t\bar{t} + ng$  for top pair production.

### 4.1 CHILI phase-space mapping

In this work, we make use of the CHILI phase-space mapping [32] to provide the map  $\phi : U \rightarrow M$ , see equation (2.2). The phase space for the final state particle  $f$  in eq. (2.19), can be expressed in terms of its transverse momentum  $p_{f,\perp}$ , rapidity  $y_f$  and azimuthal angle  $\varphi_f$  via

$$\frac{d^3\vec{p}_f}{(2\pi)^3} \frac{1}{2E_f} = \frac{1}{16\pi^2} dp_{f,\perp}^2 dy_f \frac{d\varphi_f}{2\pi}. \quad (4.1)$$

Using this parametrisation for all final-state QCD partons allows common transverse momentum and rapidity cuts to be efficiently applied. In the phase-space generation, we generate the transverse momenta according to  $dp_{f,\perp}^2 / (2p_{\perp,c} + p_{f,\perp})^2$  where  $p_{\perp,c}$  denotes an adjustable parameter used to effectively map out potential phase-space cuts. The remaining variables are distributed uniformly, the rapidity between a maximum and minimum rapidity determined by external cuts and the azimuthal angle between 0 and  $2\pi$ .

To satisfy energy-momentum conservation, we use the above mapping for all but the last final state QCD parton. The phase-space integration for the last final-state momentum is then performed in combination with the integration over the light-cone momentum fractions  $dx_{i,j}$  in eq. (2.18). This combined integration allows to trivially satisfy energy-momentum conservation, by using the remaining final-state momentum to balance transverse momenta and the initial state momenta for the overall conservation. For vector-boson production, we add an additional  $s$ -channel propagator mapping according to the well known two-body decay formula [32] with the virtuality of the intermediate particle distributed according to a Breit–Wigner distribution.

The key advantage of this mapping is its simplicity. The integrator consists of a single channel, while still performing similarly compared to more involved algorithms for a wide range of LHC processes [31]. The single-channel setup is an ideal starting point for the combination with remapping techniques using a trainable map  $\psi_\theta$ , as introduced in section 2.3, since no multi-channel and consequently more complicated techniques such as [8, 10] need to be considered.

## 4.2 PEPPER event generator

We use the Monte Carlo generator PEPPER [31, 48, 49] to perform the calculation of the perturbative scattering amplitudes. PEPPER is a novel, portable parton-level event generator with GPU acceleration, developed specifically for computationally expensive processes at the LHC.

Momentum configurations are sampled using PEPPER’s internal implementation of the CHILI phase-space generator [32]. While CHILI is comparatively simple and was thus easily ported to GPU [48], it has been shown to achieve a similar performance as more complex established generators, such as COMIX [50], which is part of the SHERPA framework [51–53].

The matrix elements as given in formula (2.20) are evaluated by summing over the colour quantum numbers, using a minimal colour decomposition [54–56]. The helicity quantum numbers are sampled instead. To achieve a good sampling efficiency, PEPPER normally samples them according to their relative contribution to the overall variance of the Monte-Carlo sample with respect to the total cross section. This optimisation is not normally correlated with the optimisation of the phase-space sampling, and is essentially equivalent to an additional dimension in the VEGAS optimiser with the number of bins being equal to the number of non-vanishing helicities  $n_{\text{hels}}$ . However, when applying the neural network based optimisation we instead jointly optimise the phase-space and helicity sampling and thus expose the optimiser not only to the correlations between the different phase-space variables, but also between these variables and the helicity.

To write out parton-level events for training the external Flow models (the VEGAS model is implemented and trained within PEPPER) we utilise PEPPER’s LHEH5 event output format. The format is based on the HDF5 database library [57], accessed through the HIGHFIVE header library [58], and has been specified in refs. [59, 60]. We extend the specification for the purpose of this study to include the random numbers for each event which are required for the training, i.e. for the phase-space point and the helicity configuration.

After model training (see section 4.4), the generated random numbers for each event must be read in by PEPPER again to evaluate the performance of the optimisation. For this, we have added a corresponding reader to PEPPER, which allows to use externally generated random numbers and phase-space weights instead of internally generated random numbers and weights.

The new input/output features have been released with version 1.2 of PEPPER. They allow for a very straightforward applications of external optimisation models via simple file-based interfaces, which are nevertheless flexible and scalable on HPC due to HDF5’s fast database structure and MPI support.

### 4.3 Event generation parameters

As discussed, the two partonic processes we study are  $d\bar{d} \rightarrow e^+e^- + ng$  (lepton pair production) and  $gg \rightarrow t\bar{t} + ng$  (top pair production) at  $\sqrt{s} = 13$  TeV. In both cases, we use the NNPDF3.0 PDF set [61] to evaluate the PDFs  $f_{i,j}$  in eq. (2.18), with the running strong coupling evaluated according to the set, using the LHAPDF6 library [62]. The renormalisation and factorisation scales are set to  $\mu_R^2 = \mu_F^2 = H_T^2/2$  for lepton pair production and  $\mu_R^2 = \mu_F^2 = H_T^2/2$  for top pair production [63]. The electroweak parameters are  $\sin^2\theta_w = 0.23155$  and  $\alpha = 1/128.80$ . We use the  $Z$  and top masses  $m_Z = 91.1876$  GeV,  $m_t = m_{\bar{t}} = 173.21$  GeV and set the  $Z$  width as  $\Gamma_Z = 2.4952$  GeV. All remaining quarks are considered to be massless.

We apply the following conventional phase-space cuts. For lepton-pair production, we require the invariant mass to satisfy  $66 \text{ GeV} \leq m_{e^+e^-} \leq 116 \text{ GeV}$ . For both processes, we require all massless final-state partons to satisfy  $p_{T,j} > 20 \text{ GeV}$ ,  $|\eta_j| < 5$  and  $\Delta R_{ij} > 0.4$ , for the transverse momentum  $p_T$  and the pseudorapidity  $\eta$  of parton  $j$ , and for the pair distance  $\Delta R$  between two partons  $i, j$ , respectively.

### 4.4 Model and training parameters

For all setups and multiplicities, the VEGAS grids have 100 bins in each dimension. The bin widths are optimised using 15 optimisation steps. The number of points is determined, such that the total number of points for the highest multiplicity becomes roughly  $3 \cdot 10^8$ . This results in  $2.5 \cdot 10^5$  training points per non-vanishing helicity configuration in the lepton pair production and  $8 \cdot 10^4$  points in the top-quark pair production case.

The NFs are optimised in 8 iterations, similar to how VEGAS is trained. In contrast to refs. [19, 64], we do not use a buffer but completely replace the data in each iteration. This allows us to separate training and data production, so that both can be made efficient independently, and to use a minimal interface to PEPPER, which only needs to read in random numbers and corresponding Jacobians and to write out weights. For the first iteration,  $10^8$  weighted events are generated with PEPPER without using any remapping. In the subsequent iterations, the trained flows are used to generate  $10^7$  nonuniform random numbers per iteration as inputs, followed by a calculation of the corresponding momenta and weights with PEPPER, which then serve as training data. An embedding layer is used to provide a continuous representation of the non-vanishing helicity configurations, with its width being equal to the number of such configurations  $n_{\text{hels}}$ . In all cases, this representation is concatenated to the other input variables and fed into the input layer of each neural network.

For the Coupling Flows, the minimal number of Coupling Layers able to model all correlations between inputs,  $2\lceil \log_2 d \rceil$  [65], is used. The implementation is based on the NFLOWS python package [66], using rational-quadratic Coupling Layers [35] with 16 spline knots per dimension. Between two Coupling Layers, the inputs are permuted with a binary permutation scheme. Each Coupling Transform is parameterised by a multi layer perceptron (MLP) with ReLU activation functions. The widths of the hidden layers are growing exponentially, such that each hidden layer has twice as many nodes as the preceding

Process	$n$	$d$	$n_{\text{hels}}$	model parameters		
				VEGAS	Coupling Flow	ODE Flow
$d\bar{d} \rightarrow e^+e^- + ng$	1	7	8	700	616 880	1 078 878
	2	10	16	1005	1 438 515	1 086 249
	3	13	32	1318	2 450 475	1 098 300
	4	16	64	1674	3 563 647	1 120 863
	5	19	128	2008	5 215 120	1 169 058
$gg \rightarrow t\bar{t} + ng$	1	7	32	724	614 402	1 092 150
	2	10	64	1053	1 571 755	1 114 713
	3	13	128	1414	2 411 499	1 162 908
	4	16	256	1839	2 844 223	1 280 799

**Table 1.** Number of parameters for the different mappings. The parameters include both the number of parameters required for the phase-space remapping and the choice of the helicity configuration. We also give the number of final-state gluons  $n$ , the resulting phase-space dimensionality  $d = 3n_{\text{out}} - 2$ , and the number of non-vanishing helicity configurations  $n_{\text{hels}}$ .

layer. Hidden layers are added until the final one has more nodes than the output layer. The size of the MLPs is thus dynamic and can vary between the Coupling Layers. For the Coupling Flows, 20% of the training data are used for validation and early stopping based on the validation loss is used. This was found necessary to avoid overfitting. The AdamW optimiser [67] is used with a batch size of  $2^{16}$  and its learning rate is decreased on plateaus. For the lowest multiplicity processes,  $e^+e^- + 1, 2$  gluons and  $t\bar{t} + 1, 2$  gluons, the initial learning rate is set to  $10^{-3}$ . However, this leads to unstable training for the higher multiplicities, requiring to decrease the learning rate. For  $e^+e^- + 3, 4, 5$  gluons and  $t\bar{t} + 3$  gluons, a value of  $10^{-4}$  is thus used. For  $t\bar{t} + 4$  gluons it is further decreased to  $10^{-5}$ .

For the ODE Flows, each vector field is implemented as an MLP with 4 hidden layers of width 512, using SELU activation functions. As proposed in ref. [68], the time  $t$  is sampled from the power-law distribution  $p_\alpha(t) \propto t^{1/(1+\alpha)}$ , with  $\alpha = 1$ . A 16-dimensional Fourier feature mapping [69] is used to encode the time parameter and the encoding is concatenated to the other input variables. The ODE Flows are trained for 600 epochs with a batch size of  $2^{19}$  using the AdamW optimiser with a learning rate of  $10^{-3}$ . Neither early stopping nor learning rate decay is used, as neither was not found to improve the results. For ODE solving, necessary for sampling and density evaluation with the flow, the DormandPrince45 solver [70] as implemented in the TORCHDYN python package [71] is used. The absolute and relative tolerances of the adaptive solver are set to  $10^{-4}$ .

For all three mappings, VEGAS, Coupling Flows and ODE Flows, the total numbers of trainable parameters for the different processes are given in table 1. The numbers increase with the dimensionality and the number of helicity configurations. Compared to the Normalizing Flows, VEGAS uses about three orders of magnitude less parameters. For the two kinds of flows, the numbers are of the same order of magnitude.

## 4.5 Evaluation

After finishing the training of the models, we freeze their parameters and generate samples of 10 million weighted events that pass the phase-space cuts for each model and each final-state jet multiplicity for both processes. For each sample, we calculate the cut efficiency (the fraction of events that pass the phase-space cuts), the relative Monte-Carlo error of the cross-section integral, the Kish effective sample size  $N_{\text{eff}}$ , eq. (2.10), and the effective unweighting efficiencies  $\epsilon_{0.01}$  and  $\epsilon_{0.001}$ . This is repeated ten times with different random seeds. Mean values and standard deviations for the different figures of merit are then estimated from these repeated samples.

## 5 Results

We present results for the mean and standard deviation of several quality metrics: phase-space cut efficiency, relative integration error, effective sample size  $N_{\text{eff}}$  and unweighting efficiencies  $\epsilon_{0.01}$  and  $\epsilon_{0.001}$ . The results are given in table 2 for both  $d\bar{d} \rightarrow e^+e^- + ng$  and  $gg \rightarrow t\bar{t} + ng$ , for the non-optimised mapping (“Identity”), a VEGAS-optimised mapping, and mappings that are implemented as Coupling Flows and ODE Flows. As discussed in section 2, these metrics capture different sampling efficiency aspects. For the relative integration error, lower values are better, while in all other cases, higher values are better. We find that our newly proposed ODE Flow method has the best performance in almost all cases. The only exception is the phase-space cut efficiency, where all optimisation methods perform well, with only small differences between them. The results for the unweighting efficiencies differ far more significantly, in particular for the computationally most difficult highest gluon multiplicities  $n$  in the study.

For  $d\bar{d} \rightarrow e^+e^- + ng$  with  $n = 5$  we find  $\epsilon_{0.01} = 3.68(5)\%$  for the ODE Flow, which is about 13 times higher than for the Coupling Flow’s  $0.29(9)\%$  and about 150 times higher compared to VEGAS’  $0.024(8)\%$ . For  $\epsilon_{0.001}$ , we find even larger improvements of 43 and 184 when comparing to the Coupling Flow and to VEGAS, respectively.

For  $gg \rightarrow t\bar{t} + ng$  with  $n = 4$ , the ODE Flow’s efficiency is  $12.53(3)\%$ , which is 8 times higher than the Coupling Flow’s  $1.6(5)\%$ , and about 17 times higher compared to VEGAS’ efficiency,  $0.74(2)\%$ . For  $\epsilon_{0.001}$ , the improvements over the Coupling Flow and VEGAS are 144 and 23, respectively, with the Coupling Flow’s efficiency falling below VEGAS’ efficiency in this case.

The unweighting efficiency improvements of the Flow-based methods over VEGAS are consistently higher for  $d\bar{d} \rightarrow e^+e^- + ng$  when compared to  $gg \rightarrow t\bar{t} + ng$  at the same  $n$ . For  $n = 4$ , we find a factor of 128 for the former and a factor of 17 for the latter. The main reason is that VEGAS performs significantly better for  $gg \rightarrow t\bar{t} + ng$ , for all  $n$ . This is not only true for the unweighting efficiency  $\epsilon$ , but to a similar degree also for the relative Monte-Carlo error, indicating that this can not be traced back to the optimisation target of VEGAS. An explanation would be that the prerequisite of VEGAS—i.e. that the distribution is factorisable into each of its dimensions—is fulfilled to a lesser degree for  $d\bar{d} \rightarrow e^+e^- + ng$ . Here, CHILI introduces an  $s$ -channel for the  $Z$ -boson resonance, and there is a more pronounced dependence on the helicity configuration.

Process	$n$	mapping	cut eff./% $\uparrow$	rel. err./% $\downarrow$	$N_{\text{eff}}/\%$ $\uparrow$	$\epsilon_{0.01}/\%$ $\uparrow$	$\epsilon_{0.001}/\%$ $\uparrow$
$d\bar{d} \rightarrow e^+e^- + ng$	1	Identity	86.88(2)	0.0943(1)	11.651(8)	3.840(6)	3.00(2)
		VEGAS	98.002(6)	0.05453(5)	25.72(2)	8.12(3)	4.24(8)
		Coupling	<b>99.927(1)</b>	<b>0.0034(2)</b>	<b>99.1(2)</b>	78.68(5)	49.4(3)
		ODE	99.886(2)	0.00364(3)	98.98(3)	<b>78.91(2)</b>	<b>57.6(2)</b>
	2	Identity	75.55(2)	0.247(6)	2.2(2)	0.23(2)	0.08(3)
		VEGAS	95.287(7)	0.0949(4)	10.52(8)	1.67(2)	0.67(5)
		Coupling	<b>99.450(2)</b>	0.02(4)	79(28)	<b>48.7(6)</b>	13(5)
		ODE	98.383(6)	<b>0.00990(9)</b>	<b>92.8(2)</b>	35.0(2)	<b>15.5(2)</b>
	3	Identity	65.04(2)	1.4(9)	0.15(8)	0.007(7)	0.003(2)
		VEGAS	<b>92.75(2)</b>	0.175(3)	3.4(1)	0.32(2)	0.10(3)
		Coupling	92.48(2)	0.030(7)	58(9)	15.5(2)	3.0(7)
		ODE	90.60(1)	<b>0.02085(6)</b>	<b>77.2(2)</b>	<b>22.28(6)</b>	<b>11.0(2)</b>
	4	Identity	55.18(2)	2.8(9)	0.02(1)	0.0011(6)	0.0011(6)
		VEGAS	<b>88.87(2)</b>	0.32(2)	1.1(2)	0.07(1)	0.02(1)
		Coupling	85.24(1)	0.053(3)	31(2)	4.43(7)	1.1(2)
		ODE	83.099(9)	<b>0.0386(2)</b>	<b>48.7(3)</b>	<b>8.96(4)</b>	<b>3.95(9)</b>
	5	Identity	46.09(2)	8(7)	0.004(3)	0.0004(2)	0.0004(2)
		VEGAS	<b>84.29(1)</b>	0.52(4)	0.4(1)	0.024(8)	0.007(3)
		Coupling	82.90(2)	0.2(1)	4(2)	0.29(9)	0.03(3)
		ODE	77.69(2)	<b>0.061(4)</b>	<b>28(2)</b>	<b>3.68(5)</b>	<b>1.29(8)</b>
$g\bar{g} \rightarrow t\bar{t} + ng$	1	Identity	77.70(2)	0.2352(6)	2.29(2)	0.434(6)	0.27(2)
		VEGAS	98.368(4)	0.05358(6)	26.27(4)	7.10(5)	3.2(1)
		Coupling	<b>99.9943(3)</b>	<b>0.00466(3)</b>	<b>97.92(3)</b>	<b>67.17(4)</b>	<b>45.6(3)</b>
		ODE	99.9843(4)	0.00515(5)	97.47(5)	65.21(3)	45.50(9)
	2	Identity	65.40(2)	0.47(2)	0.68(3)	0.063(5)	0.021(7)
		VEGAS	95.997(6)	0.0676(2)	18.70(4)	3.55(2)	1.49(4)
		Coupling	<b>99.205(3)</b>	<b>0.013(2)</b>	<b>85(2)</b>	<b>35.9(2)</b>	10.2(9)
		ODE	98.328(5)	0.0205(3)	71.7(5)	24.39(4)	<b>13.35(8)</b>
	3	Identity	54.27(3)	1.1(2)	0.13(3)	0.008(3)	0.003(1)
		VEGAS	92.640(9)	0.0904(3)	11.79(8)	1.60(2)	0.59(4)
		Coupling	<b>94.008(6)</b>	<b>0.0246(2)</b>	<b>66.4(4)</b>	<b>15.26(6)</b>	6.3(3)
		ODE	93.68(2)	0.02768(4)	60.49(6)	<b>15.26(3)</b>	<b>8.7(2)</b>
	4	Identity	44.36(2)	3(1)	0.03(2)	0.0011(8)	0.0010(7)
		VEGAS	88.304(8)	0.123(1)	7.0(1)	0.74(2)	0.23(3)
		Coupling	<b>91.269(5)</b>	0.2(2)	8(6)	1.6(5)	0.04(6)
		ODE	88.456(8)	<b>0.0300(2)</b>	<b>59.6(5)</b>	<b>12.53(3)</b>	<b>5.76(9)</b>

**Table 2.** Comparison of different mappings for the  $g\bar{g} \rightarrow t\bar{t} + ng$  example using samples with 10M nonzero weight events. The relative error of the total cross section estimate has been determined from 10M events including zero weights. The uncertainties have been obtained as the standard deviation of 10 independent samples generated with the same mapping (without re-training). All errors and uncertainties are rounded up in the last digit given.

In terms of the relative integration error, we find similar improvements. The Normalizing Flows achieve significant improvements for all multiplicities considered. For  $d\bar{d} \rightarrow e^+e^- + ng$  with  $n = 5$  we find a value of 0.061(4) % for the ODE Flow, which is about 3 times less than the Coupling Flow and about 9 times less than VEGAS. Considering that the integral error scales as  $1/\sqrt{N}$  we need to square these numbers to determine the improvement in efficiency, i.e. the reduction in the number of points needed to determine the integral with the same error. This results in factors of 11 and 73, respectively, in comparison to the Coupling Flow and VEGAS. The corresponding factors for  $gg \rightarrow t\bar{t} + ng$  with  $n = 4$  are 44 and 17, where in analogy to the results for the unweighting efficiency the Coupling Flow produces a larger error than VEGAS. Over all multiplicities, the improvements range between 14 and 224.

The effective sample size also benefits significantly from the Normalizing Flows. While the identity mapping achieves values of  $N_{\text{eff}} > 1\%$  only for the lowest multiplicities, VEGAS achieves this in all cases except  $d\bar{d} \rightarrow e^+e^- + 5g$ . The Normalizing Flows, however, lead to much higher values and with the ODE Flow the effective sample size is above 25 % in all cases considered. In accordance with the results for the unweighting efficiency and the relative integration error, the highest multiplicities favour the ODE Flow over the Coupling Flow. For the lowest multiplicity,  $n = 1$ , the effective sample size with the Normalizing Flows is close to 100 %. Accordingly, the improvement with respect to VEGAS, which achieves about 25 %, is close to the maximum factor of about 4. The improvement factor increases with multiplicity and is highest for  $d\bar{d} \rightarrow e^+e^- + 5g$ , where the ODE Flow produces a 70 times larger effective sample size in comparison to VEGAS. With respect to the Coupling Flow, the factor is about 9 in this case.

The improved sampling by the ODE Flow method also manifests itself in a narrower weight distribution, as shown in figure 2 for  $d\bar{d} \rightarrow e^+e^- + ng$  with  $n = 5$  (left) and  $gg \rightarrow t\bar{t} + ng$  with  $n = 4$  (right). A narrower distribution is directly related to a larger effective sample size  $N_{\text{eff}}$ . As discussed in section 2.3, for a good unweighting efficiency the most relevant feature of the weight distribution is the steepness of its tail towards large values  $w$ , since this will determine the value of the denominator,  $w_{\text{max,eff}}$ , in eq. (2.9). Indeed, the ODE Flow yields a significantly steeper right tail in the weight distribution for both cases, compared to the other methods including the Coupling Flows.

To study the scaling behaviour with the number of final-state gluons  $n$ , we compare the values of  $\epsilon_{0.001}$  in figure 3. We find that the ratio of the efficiency for the ODE Flow over the efficiency of VEGAS generally increases with  $n$ . On the other hand, the Coupling Flows at first show similar improvements over VEGAS, but for the largest  $n$  decrease in efficiency significantly, for both processes, indicating an unfavourable scaling behaviour towards large  $n$ . By evaluating the training results ten times with different random seeds, we can plot spreads for the data points. We find that they are smallest for the ODE Flows, which means that this method generates the fewest very large event weight outliers.

Finally, we analyse the convergence behaviour of  $\epsilon_{0.001}$  as a function of training iterations in figure 4 for the highest multiplicity of each process. We find that all methods are reasonably converged at their last iteration. The spread of their results over ten independent samples is consistently the smallest for the ODE Flows towards later iterations, with good stability from one optimisation step to the next. We observe that the VEGAS results are less stable

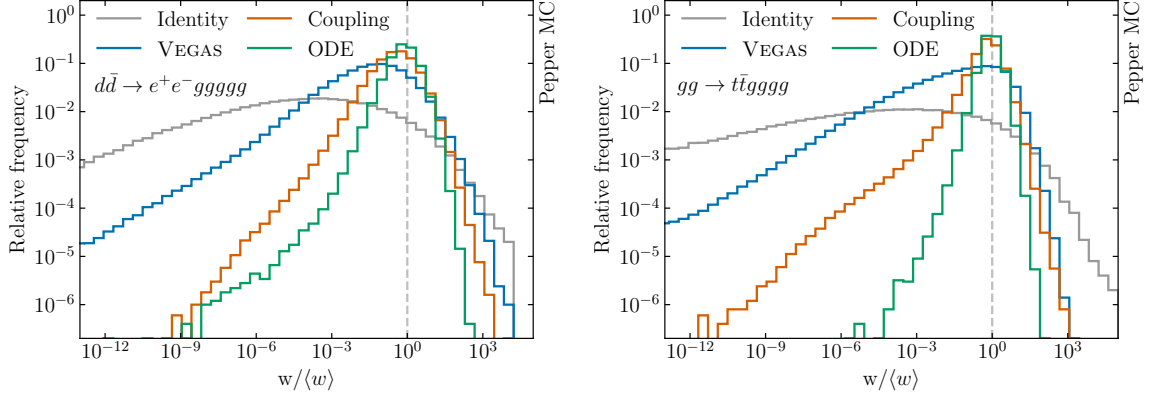


**Figure 2.** Normalised weight distributions for  $5 \cdot 10^6$  points for the  $e^+e^- + 5$  gluons example (left) and the  $t\bar{t} + 4$  gluons example (right). The plotted weights include matrix-element and phase-space weights, as well as PDF and, where applicable, the Jacobian of the remapping. Distributions are shown for the “Identity” mapping, and mappings optimised by VEGAS, Coupling Flows (“Coupling”), and ODE Flows (“ODE”).

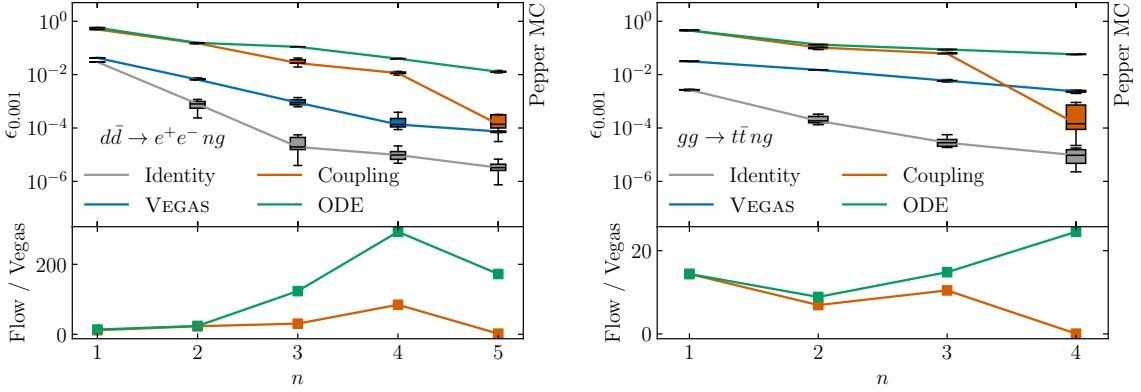


**Figure 3.** Unweighting efficiencies  $\epsilon_{0.001}$  for the  $e^+e^- + n$  gluons example (left) and the  $t\bar{t} + n$  gluons example (right), for various gluon multiplicities  $n$ . The efficiencies are shown for the “Identity” mapping, and mappings optimised by VEGAS, Coupling Flows (“Coupling”), and ODE Flows (“ODE”). Each curve represents the mean over ten independent evaluations of the unweighting efficiency, the boxes indicate the quartiles of the distribution and the whiskers show  $3/2$  of the interquartile range.

for  $d\bar{d} \rightarrow e^+e^- + ng$  when compared to  $gg \rightarrow t\bar{t} + ng$ , consistent with the lower overall performance we have observed earlier for the former process. Also the Coupling Flows give numerically less stable results when compared to the ODE Flows, with a larger spread of results, indicating a larger fraction of outliers with large weights affecting the  $w_{\max, \text{eff}}$  determination. This might be an effect of the Coupling Flow’s MLE objective versus the regression-based Flow Matching objective.

The above observations support the conclusion that the new Flow Matching based method performs best, in particular in the most relevant metrics for event generation, the unweighting efficiency. The advantage over the Coupling Flow based approach is most pronounced at the highest multiplicities studied, where the performance of the Coupling

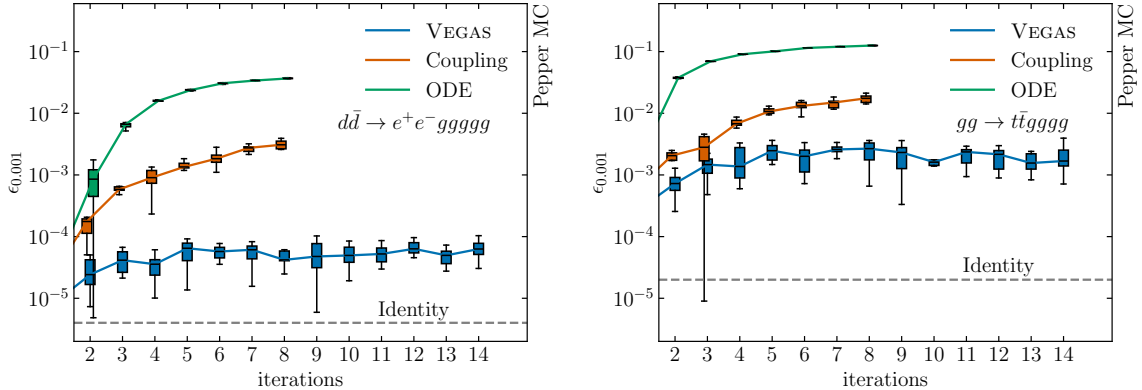


**Figure 4.** Convergence of the effective unweighting efficiency  $\epsilon_{0.001}$  with training iterations for the highest final-state gluon multiplicities studied:  $d\bar{d} \rightarrow e^+e^- + 5g$  (left) and  $gg \rightarrow t\bar{t} + 4g$  (right). Results are shown for the “Identity” mapping, Vegas, Coupling Flow (“Coupling”), and ODE Flow (“ODE”). Each curve represents the mean over ten independent evaluations of the unweighting efficiency, the boxes indicate the quartiles of the distribution and the whiskers show  $3/2$  of the interquartile range.

Flows drops significantly. This observation is consistent with others, which empirically show that time-discrete flows trained with MLE fall short in terms of expressivity and scalability [72]. Since the highest multiplicities drive the computational cost of event generation for current state-of-the-art production campaigns at the LHC, using a Flow Matching based approach would be highly beneficial.

## 6 Conclusion

We have presented the first application of the Flow Matching method to the problem of high-dimensional phase-space sampling in high-energy particle physics. The model is trained not only on the continuous kinematic phase-space dimensions, but also on the discrete variable used to select a helicity configuration. The training of the model and testing it in production is facilitated by a newly implemented simple file-based interface in the event generator PEPPER. The interface builds on the LHEH5 parton-level event database format, and is used to train the model and then test it in production. The interface is simple and can be used in the future to study more applications and also other novel sampling methods in a straightforward way.

In this contribution, we studied Drell–Yan and top–antitop pair production. Specifically, we evaluated various sampling efficiency metrics for the most challenging partonic channels  $d\bar{d} \rightarrow e^+e^- + ng$  with  $1 \leq n \leq 5$  and  $gg \rightarrow t\bar{t} + ng$  with  $1 \leq n \leq 4$ . The upper limits of these multiplicity ranges correspond to the highest number of jets currently simulated at the matrix-element level for experimental analyses. Their high complexity and low phase-space efficiency render them the main bottlenecks in current large-scale state-of-the-art event generation campaigns. The key performance metric for these productions is the unweighting efficiency  $\epsilon_{0.01}$ . Here, we find gain factors of 150 (17) for  $d\bar{d} \rightarrow e^+e^- + ng$  with  $n = 5$  ( $gg \rightarrow t\bar{t} + ng$  with  $n = 4$ ). These substantial improvements can be directly translated

into increased parton-level event generation throughput. Overall, these results represent a significant advancement in the scalability and efficiency of event generation for experimental physics analyses.

This study focused on the computationally most expensive partonic channel of each process. However, realistic simulations require the inclusion of all partonic channels during both training and generation. In a future work, we aim to develop a single conditional model that can simultaneously sample from all partonic channels. This combined approach enables the model to leverage correlations between channels, improving training effectiveness. Similar correlations also exist across different jet multiplicities. Consequently, a complementary strategy is to investigate the joint training of all multiplicities within a single model to further enhance training efficiency and production performance. Another improvement would be the use of rectification methods [28, 44, 45] that straighten the flow trajectories. These have the potential to significantly reduce the cost of the Flow sampling.

## Acknowledgments

The authors gratefully acknowledge the computing time granted by the Resource Allocation Board and provided on the supercomputer Emmy/Grete at NHR-Nord@Göttingen as part of the NHR infrastructure. The calculations for this research were conducted with computing resources under the project nhr\_ni\_starter\_22045. The authors also acknowledge the use of computing resources made available by CERN to conduct some of the research reported in this work. This material is based upon work supported by Fermi Forward Discovery Group, LLC under Contract No. 89243024CSC000002 with the U.S. Department of Energy, Office of Science, Office of High Energy Physics. EB and MK acknowledge support by the Deutsche Forschungsgemeinschaft (DFG, German Research Foundation) – 510810461. TJ acknowledges financial support from the German Federal Ministry of Education and Research (BMBF) in the ErUM-Data action plan through the KISS consortium (Verbundprojekt 05D2022). BS and FHS were supported by the German Research Foundation (DFG) SFB 1456, Mathematics of Experiment – Project-ID 432680300. BS was supported by the Emmy Noether Programme of the DFG – Project-ID 403056140.

## A Event generation runcards

The PEPPER v1.3 event generator<sup>3</sup> runcards that were used for this project are given in listings 1 and 2. In addition to using the runcards, the code needs to be compiled after changing the line `#define HELICITY_BLOCK_SIZE 32` to `#define HELICITY_BLOCK_SIZE 1` in `src/event_data.h`, to avoid the generation of blocks of correlated events that share a given helicity configuration.

The runcards were used to generate the VEGAS and non-optimised “Identity” baseline results, to generate the training data for the Flow models and then to measure the performance of the trained models. For the latter, the runcard line for the `input_path` setting should be used (by removing the semicolon to uncomment the line), to enable reading the random

---

<sup>3</sup><https://gitlab.com/spice-mc/pepper/-/releases/1.3.0-kokkos>

```

[main]
process = d db -> e+ e- g g g g g
mu2 = H_Tp^2/2
; helicity_integrator = false

[events]
random_numbers_output_enabled = true
unweighting_disabled = true
output_path = training_data_for_flow_model.hdf5
; input_path = random_numbers_from_flow_model.hdf5

[phase_space.vegas]
; disabled = true
alpha = 0.8

[phase_space.optimisation]
n_iter = 15
n_nonzero_min = 250000
n_nonzero_min_growth_factor = 1.00

```

Listing 1: The PEPPER runcard used for generating  $d\bar{d} \rightarrow e^+e^- gggg$  events. For generating a different number of final-state gluons, only the `process` setting needs to be adjusted.

numbers generated by the model, instead of relying on PEPPER’s internal random-number generator.

## B Additional figures

In this appendix, we present figures analogous to figure 3 and figure 4, but for  $\epsilon_{0.01}$  instead of  $\epsilon_{0.001}$ . figure 5 displays the unweighting efficiency as a function of the number of additional final-state gluons, for both the  $e^+e^- + n$  gluons and  $t\bar{t} + n$  gluons processes, corresponding to figure 3. Similarly, figure 6 shows the convergence behaviour of the unweighting efficiency for  $\epsilon_{0.01}$ , in correspondence with figure 4.

## References

- [1] EUROPEAN STRATEGY GROUP collaboration, *2020 Update of the European Strategy for Particle Physics*, CERN Council, Geneva (2020), [10.17181/ESU2020](#).
- [2] M. Narain et al., *The Future of US Particle Physics - The Snowmass 2021 Energy Frontier Report*, [2211.11084](#).
- [3] HEP SOFTWARE FOUNDATION collaboration, *A Roadmap for HEP Software and Computing R&D for the 2020s*, *Comput. Softw. Big Sci.* **3** (2019) 7 [[1712.06982](#)].
- [4] HSF PHYSICS EVENT GENERATOR WG collaboration, *Challenges in Monte Carlo Event Generator Software for High-Luminosity LHC*, *Comput. Softw. Big Sci.* **5** (2021) 12 [[2004.13687](#)].

```

[main]
process = g g -> t tb g g g g
mu2 = H_T^2/2
; helicity_integrator = false

[events]
random_numbers_output_enabled = true
unweighting_disabled = true
output_path = training_data_for_flow_model.hdf5
; input_path = random_numbers_from_flow_model.hdf5

[phase_space.vegas]
; disabled = true
alpha = 0.8

[phase_space.optimisation]
n_iter = 15
n_nonzero_min = 80000
n_nonzero_min_growth_factor = 1.00

```

Listing 2: The PEPPER runcard used for generating  $gg \rightarrow t\bar{t}ggg$  events. For generating a different number of final-state gluons, only the `process` setting needs to be adjusted.

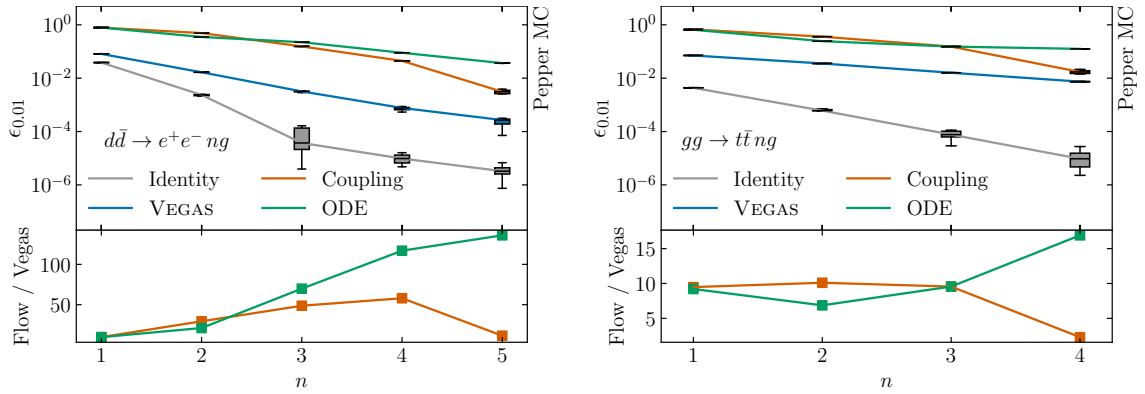


**Figure 5.** Unweighting efficiencies,  $\epsilon_{0.01}$  for the  $e^+e^- + n$  gluons example (left) and the  $t\bar{t} + n$  gluons example (right), for various gluon multiplicities  $n$ . The efficiencies are shown for the “Identity” mapping, and mappings optimised by VEGAS, Coupling Flows (“Coupling”), and ODE Flows (“ODE”).

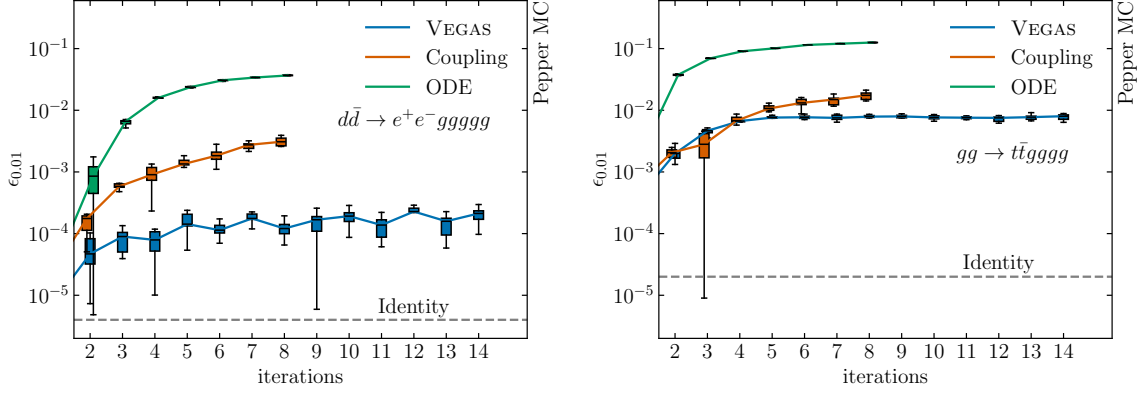


**Figure 6.** Convergence of the effective unweighting efficiency  $\epsilon_{0.01}$  with training iterations for the highest final-state gluon multiplicities studied:  $d\bar{d} \rightarrow e^+e^- + 5g$  (left) and  $gg \rightarrow t\bar{t} + 4g$  (right). Results are shown for the “Identity” mapping, Vegas, Coupling Flow (“Coupling”), and ODE Flow (“ODE”). Each curve represents the mean over ten independent evaluations of the unweighting efficiency, the boxes indicate the quartiles of the distribution and the whiskers show  $3/2$  of the interquartile range.

- [5] HSF PHYSICS EVENT GENERATOR WG collaboration, *HL-LHC Computing Review Stage-2, Common Software Projects: Event Generators*, [2109.14938](#).
- [6] ATLAS collaboration, *Modelling and computational improvements to the simulation of single vector-boson plus jet processes for the ATLAS experiment*, *JHEP* **08** (2022) 089 [[2112.09588](#)].
- [7] E. Bothmann, A. Buckley, I.A. Christidi, C. Gütschow, S. Höche, M. Knobbe et al., *Accelerating LHC event generation with simplified pilot runs and fast PDFs*, *Eur. Phys. J. C* **82** (2022) 1128 [[2209.00843](#)].
- [8] R. Kleiss and R. Pittau, *Weight optimization in multichannel Monte Carlo*, *Comput. Phys. Commun.* **83** (1994) 141 [[hep-ph/9405257](#)].
- [9] G.P. Lepage, *A New Algorithm for Adaptive Multidimensional Integration*, *J. Comput. Phys.* **27** (1978) 192.
- [10] T. Ohl, *Vegas revisited: Adaptive Monte Carlo integration beyond factorization*, *Comput. Phys. Commun.* **120** (1999) 13 [[hep-ph/9806432](#)].
- [11] G.P. Lepage, *Adaptive multidimensional integration: VEGAS enhanced*, *J. Comput. Phys.* **439** (2021) 110386 [[2009.05112](#)].
- [12] S. Jadach, *Foam: A General purpose cellular Monte Carlo event generator*, *Comput. Phys. Commun.* **152** (2003) 55 [[physics/0203033](#)].
- [13] T. Hahn, *CUBA: A Library for multidimensional numerical integration*, *Comput. Phys. Commun.* **168** (2005) 78 [[hep-ph/0404043](#)].
- [14] A. van Hameren, *PARNI for importance sampling and density estimation*, *Acta Phys. Polon. B* **40** (2009) 259 [[0710.2448](#)].
- [15] S. Höche, S. Prestel and H. Schulz, *Simulation of Vector Boson Plus Many Jet Final States at the High Luminosity LHC*, *Phys. Rev. D* **100** (2019) 014024 [[1905.05120](#)].
- [16] M.D. Klimek and M. Perelstein, *Neural Network-Based Approach to Phase Space Integration*, *SciPost Phys.* **9** (2020) 053 [[1810.11509](#)].

- [17] E. Bothmann, T. Janßen, M. Knobbe, T. Schmale and S. Schumann, *Exploring phase space with Neural Importance Sampling*, *SciPost Phys.* **8** (2020) 069 [[2001.05478](#)].
- [18] C. Gao, S. Höche, J. Isaacson, C. Krause and H. Schulz, *Event Generation with Normalizing Flows*, *Phys. Rev. D* **101** (2020) 076002 [[2001.10028](#)].
- [19] T. Heimel, R. Winterhalder, A. Butter, J. Isaacson, C. Krause, F. Maltoni et al., *MadNIS - Neural multi-channel importance sampling*, *SciPost Phys.* **15** (2023) 141 [[2212.06172](#)].
- [20] R. Verheyen, *Event Generation and Density Estimation with Surjective Normalizing Flows*, *SciPost Phys.* **13** (2022) 047 [[2205.01697](#)].
- [21] T. Heimel, N. Huetsch, F. Maltoni, O. Mattelaer, T. Plehn and R. Winterhalder, *The MadNIS reloaded*, *SciPost Phys.* **17** (2024) 023 [[2311.01548](#)].
- [22] T. Heimel, O. Mattelaer, T. Plehn and R. Winterhalder, *Differentiable MadNIS-Lite*, *SciPost Phys.* **18** (2025) 017 [[2408.01486](#)].
- [23] S. Badger et al., *Machine learning and LHC event generation*, *SciPost Phys.* **14** (2023) 079 [[2203.07460](#)].
- [24] R.T.Q. Chen, Y. Rubanova, J. Bettencourt and D. Duvenaud, *Neural ordinary differential equations*, in *Proceedings of the 32nd International Conference on Neural Information Processing Systems*, NeurIPS'18, (Red Hook, NY, USA), p. 6572–6583, Curran Associates Inc., 2018 [[1806.07366](#)].
- [25] Y. Lipman, R.T.Q. Chen, H. Ben-Hamu, M. Nickel and M. Le, *Flow matching for generative modeling*, [2210.02747](#).
- [26] M.S. Albergo and E. Vanden-Eijnden, *Building normalizing flows with stochastic interpolants*, in *The Eleventh International Conference on Learning Representations*, 2023 [[2209.15571](#)].
- [27] M.S. Albergo, N.M. Boffi and E. Vanden-Eijnden, *Stochastic interpolants: A unifying framework for flows and diffusions*, [2303.08797](#).
- [28] X. Liu, C. Gong and Q. Liu, *Flow straight and fast: Learning to generate and transfer data with rectified flow*, [2209.03003](#).
- [29] A. Butter, N. Huetsch, S. Palacios Schweitzer, T. Plehn, P. Sorrenson and J. Spinner, *Jet Diffusion versus JetGPT – Modern Networks for the LHC*, [2305.10475](#).
- [30] L. Favaro, R. Kogler, A. Paasch, S. Palacios Schweitzer, T. Plehn and D. Schwarz, *How to Unfold Top Decays*, [2501.12363](#).
- [31] E. Bothmann, T. Childers, W. Giele, S. Höche, J. Isaacson and M. Knobbe, *A portable parton-level event generator for the high-luminosity LHC*, *SciPost Phys.* **17** (2024) 081 [[2311.06198](#)].
- [32] E. Bothmann, T. Childers, W. Giele, F. Herren, S. Hoeche, J. Isaacson et al., *Efficient phase-space generation for hadron collider event simulation*, *SciPost Phys.* **15** (2023) 169 [[2302.10449](#)].
- [33] L. Dinh, D. Krueger and Y. Bengio, *NICE: non-linear independent components estimation*, in *3rd International Conference on Learning Representations, ICLR 2015, San Diego, CA, USA, May 7-9, 2015, Workshop Track Proceedings*, Y. Bengio and Y. LeCun, eds., 2015, <http://arxiv.org/abs/1410.8516> [[1410.8516](#)].
- [34] T. Müller, B. McWilliams, F. Rousselle, M. Gross and J. Novák, *Neural importance sampling*, *ACM Trans. Graph.* **38** (2019) [[1808.03856](#)].

- [35] C. Durkan, A. Bekasov, I. Murray and G. Papamakarios, *Neural spline flows*, in *Advances in Neural Information Processing Systems*, H. Wallach, H. Larochelle, A. Beygelzimer, F. d'Alché-Buc, E. Fox and R. Garnett, eds., vol. 32, Curran Associates, Inc., 2019 [[1906.04032](#)].
- [36] J. von Neumann, *John von Neumann Collected Works*, vol. 5: Design of Computers, Theory of Automata and Numerical Analysis, (Oxford, England), pp. 768–770, Pergamon Press (1961).
- [37] L. Kish, *Survey Sampling*, Wiley (1965).
- [38] E. Tabak and E. Vanden-Eijnden, *Density estimation by dual ascent of the log-likelihood*, *Communications in Mathematical Sciences - COMMUN MATH SCI* **8** (2010) .
- [39] E.G. Tabak and C.V. Turner, *A family of nonparametric density estimation algorithms*, *Communications on Pure and Applied Mathematics* **66** (2013) 145.
- [40] B. Stienen and R. Verheyen, *Phase space sampling and inference from weighted events with autoregressive flows*, *SciPost Phys.* **10** (2021) 038 [[2011.13445](#)].
- [41] N. Deutschmann and N. Götz, *Accelerating HEP simulations with Neural Importance Sampling*, *JHEP* **03** (2024) 083 [[2401.09069](#)].
- [42] C. Finlay, J.-H. Jacobsen, L. Nurbekyan and A.M. Oberman, *How to train your neural ode: the world of jacobian and kinetic regularization*, in *Proceedings of the 37th International Conference on Machine Learning*, ICML'20, JMLR.org, 2020 [[2002.02798](#)].
- [43] D. Onken, S.W. Fung, X. Li and L. Ruthotto, *OT-Flow: Fast and accurate continuous normalizing flows via optimal transport*, in *AAAI Conference on Artificial Intelligence*, vol. 35, pp. 9223–9232, May, 2021, <https://ojs.aaai.org/index.php/AAAI/article/view/17113> [[2006.00104](#)].
- [44] A. Tong, K. FATRAS, N. Malkin, G. Huguet, Y. Zhang, J. Rector-Brooks et al., *Improving and generalizing flow-based generative models with minibatch optimal transport*, *Transactions on Machine Learning Research* (2024) [[2302.00482](#)].
- [45] A.-A. Pooladian, H. Ben-Hamu, C. Domingo-Enrich, B. Amos, Y. Lipman and R.T.Q. Chen, *Multisample flow matching: straightening flows with minibatch couplings*, in *Proceedings of the 40th International Conference on Machine Learning*, ICML'23, JMLR.org, 2023 [[2304.14772](#)].
- [46] S. La Cagnina, C. Grunwald, T. Janßen, K. Kröninger and S. Schumann, *Phase space sampling with Markov Chain Monte Carlo methods*, 12, 2024 [[2412.12963](#)].
- [47] T. Janßen, R. Poncelet and S. Schumann, *Sampling NNLO QCD phase space with normalizing flows*, [2505.13608](#).
- [48] E. Bothmann, W. Giele, S. Hoeche, J. Isaacson and M. Knobbe, *Many-gluon tree amplitudes on modern GPUs: A case study for novel event generators*, *SciPost Phys. Codeb.* **2022** (2022) 3 [[2106.06507](#)].
- [49] E. Bothmann, J. Isaacson, M. Knobbe, S. Höche and W. Giele, *QCD tree amplitudes on modern GPUs: A case study for novel event generators*, *PoS ICHEP2022* (2022) 222.
- [50] T. Gleisberg and S. Hoeche, *Comix, a new matrix element generator*, *JHEP* **12** (2008) 039 [[0808.3674](#)].
- [51] T. Gleisberg, S. Höche, F. Krauss, M. Schönherr, S. Schumann, F. Siegert et al., *Event generation with SHERPA 1.1*, *JHEP* **02** (2009) 007 [[0811.4622](#)].

- [52] SHERPA collaboration, *Event Generation with Sherpa 2.2*, *SciPost Phys.* **7** (2019) 034 [[1905.09127](#)].
- [53] SHERPA collaboration, *Event generation with Sherpa 3*, *JHEP* **12** (2024) 156 [[2410.22148](#)].
- [54] T. Melia, *Dyck words and multi-quark primitive amplitudes*, *Phys. Rev. D* **88** (2013) 014020 [[1304.7809](#)].
- [55] T. Melia, *Dyck words and multi-quark amplitudes*, *PoS RADCOR2013* (2013) 031.
- [56] H. Johansson and A. Ochirov, *Color-Kinematics Duality for QCD Amplitudes*, *JHEP* **01** (2016) 170 [[1507.00332](#)].
- [57] The HDF Group, *Hierarchical Data Format, version 5*, <https://www.hdfgroup.org/HDF5/>.
- [58] *HighFive - HDF5 header-only C++ Library*, <https://bluebrain.github.io/HighFive/>.
- [59] S. Höche, S. Prestel and H. Schulz, *Simulation of Vector Boson Plus Many Jet Final States at the High Luminosity LHC*, *Phys. Rev.* **D100** (2019) 014024 [[1905.05120](#)].
- [60] E. Bothmann, T. Childers, C. Gütschow, S. Höche, P. Hovland, J. Isaacson et al., *Efficient precision simulation of processes with many-jet final states at the LHC*, *Phys. Rev. D* **109** (2024) 014013 [[2309.13154](#)].
- [61] NNPDF collaboration, *Parton distributions for the LHC Run II*, *JHEP* **04** (2015) 040 [[1410.8849](#)].
- [62] A. Buckley, J. Ferrando, S. Lloyd, K. Nordström, B. Page, M. Rüfenacht et al., *LHAPDF6: parton density access in the LHC precision era*, *Eur. Phys. J. C* **75** (2015) 132 [[1412.7420](#)].
- [63] Z. Bern, L.J. Dixon, F. Febres Cordero, S. Höche, H. Ita, D.A. Kosower et al., *Next-to-Leading Order  $W + 5$ -Jet Production at the LHC*, *Phys. Rev. D* **88** (2013) 014025 [[1304.1253](#)].
- [64] T. Akhond-Sadegh, J. Rector-Brooks, A. Joey Bose, S. Mittal, P. Lemos, C.-H. Liu et al., *Iterated denoising energy matching for sampling from boltzmann densities*, in *Proceedings of the 41st International Conference on Machine Learning, ICML'24, JMLR.org, 2024* [[2402.06121](#)].
- [65] C. Gao, J. Isaacson and C. Krause, *i-flow: High-dimensional Integration and Sampling with Normalizing Flows*, *Mach. Learn. Sci. Tech.* **1** (2020) 045023 [[2001.05486](#)].
- [66] C. Durkan, A. Bekasov, I. Murray and G. Papamakarios, *nflows: normalizing flows in PyTorch*, Zenodo (2020), [10.5281/zenodo.4296287](https://zenodo.org/record/4296287).
- [67] I. Loshchilov and F. Hutter, *Decoupled weight decay regularization*, in *7th International Conference on Learning Representations, ICLR 2019, New Orleans, LA, USA, May 6-9, 2019*, OpenReview.net, 2019 [[1711.05101](#)].
- [68] J. Wildberger, M. Dax, S. Buchholz, S.R. Green, J.H. Macke and B. Schölkopf, *Flow matching for scalable simulation-based inference*, in *Proceedings of the 37th International Conference on Neural Information Processing Systems, NeurIPS '23, (Red Hook, NY, USA), Curran Associates Inc., 2023* [[2305.17161](#)].
- [69] M. Tancik, P.P. Srinivasan, B. Mildenhall, S. Fridovich-Keil, N. Raghavan, U. Singhal et al., *Fourier features let networks learn high frequency functions in low dimensional domains*, in *Proceedings of the 34th International Conference on Neural Information Processing Systems, NeurIPS '20, (Red Hook, NY, USA), Curran Associates Inc., 2020* [[2006.10739](#)].
- [70] J. Dormand and P. Prince, *A family of embedded runge-kutta formulae*, *Journal of Computational and Applied Mathematics* **6** (1980) 19.

- [71] M. Poli, S. Massaroli, A. Yamashita, H. Asama, J. Park and S. Ermon, *Torchdyn: Implicit models and neural numerical methods in pytorch*, <https://github.com/DiffEqML/torchdyn>.
- [72] D. Rehman, O. Davis, J. Lu, J. Tang, M. Bronstein, Y. Bengio et al., *Fort: Forward-only regression training of normalizing flows*, [2506.01158](https://arxiv.org/abs/2506.01158).